Arabian Journal of Chemistry (2023) **16**, 105069

King Saud University

Arabian Journal of Chemistry

www.ksu.edu.sa
www.sciencedirect.com

ORIGINAL ARTICLE

Synergistic effect of surface reconstruction and rGO for FeS_2/rGO electrocatalysis with efficient oxygen evolution reaction for water splitting

Xiaozhen Ren [a,*], Shanshan Li [a], Junchang Liu [a], Yanan Zhou [a], Jie Yin [a], Hua Yang [b,*]

[a] *School of Materials Science and Engineering, Liaocheng University, Liaocheng 252000, China*
[b] *School of Chemistry, Jilin University, Changchun 130012, China*

Received 28 March 2023; accepted 8 June 2023
Available online 13 June 2023

KEYWORDS

Iron sulfide;
Self reconstruction;
Electron transfer channel;
Water splitting;
Synergistic effect

Abstract Exploring highly active and inexpensive electrocatalysts for oxygen evolution is vital but challenging. Herein, a serial of FeS_2, FeS and FeS_2/rGO electrocatalysts were obtained by simple two-step method. Benefiting from the integration of FeS_2 and rGO, the FeS_2-450/rGO-10% exhibited the excellent catalytic activity toward OER with an ultra-low overpotential of 140 mV, a smaller Tafel slope of 71 mV/dec and high stability. The improved catalytic performance for OER could attribute to the excellent synergistic effect of the surface reconstruction of FeS_2 and the introduction of rGO in FeS_2-450/rGO-10% catalyst. Meanwhile, in a two-electrode system of FeS_2-450/rGO-10%/NF//Pt/C/NF toward overall water splitting, the voltage at 10 mA cm^{-2} is only 1.52 mV, which indicates that the FeS_2-450/rGO-10% can serve as the anode in practical overall water splitting.

1. Introduction

To approach carbon neutrality by 2050/2060, it is urgent to develop clean energy. As a kind of green and pollution-free energy, hydrogen energy has received more and more attention. Electrochemical water splitting, which contains two half reactions: the oxygen evolution reaction (OER) and hydrogen evolution reaction (HER), is one of an effective way to produce hydrogen energy (Wang et al., 2023; Wu et al., 2022). Compared with HER, OER is more complicated due to its slow-moving kinetics of four electrons transfer, which needs large overpotential (Li et al., 2018a; Xu et al., 2021). Therefore, we should pay much attention to explore a suitable catalyst to reduce the energy barrier for OER. Up to now, noble metal-based materials, such as InO_2 or RuO_2, are the state-of-the-art OER electrocatalysts because of their

* Corresponding authors at: 1 Hunan Road, Liaocheng City, Shandong Province, China (Xiaozhen Ren). 2699 Qianjin Dajie, Chaoyang District, Changchun City, Jilin Province, China (Hua Yang).
E-mail addresses: renxiaozhen@lcu.edu.cn (X. Ren), huayang86@-sina.com (H. Yang).
Peer review under responsibility of King Saud University.

Production and hosting by Elsevier

https://doi.org/10.1016/j.arabjc.2023.105069
1878-5352

high efficiency (Audichon et al., 2016; Wu et al., 2016). Whereas, their widespread practical production has been severely inhibited due to the scarcity and high price. Therefore, we must explore highly cost-efficient and earth-abundant OER electrocatalysts for practical application.

Among a wide variety of noble metal-free electrocatalysts for OER, transition metal-based nanomaterials having high catalytic activity are promising alternatives, such as transition metal oxides (Gao et al., 2014), carbides (Roy et al., 2021), nitrides (Li et al., 2022), sulfides (Jiang et al., 2021; Ren et al., 2022) and phosphides (Jin et al., 2014). Many strategies, such as defecting regulation, heterostructure construction and morphology engineering *et al.* have been used to improve their OER activity and stability. Meanwhile, some researchers have focused on the surface structure, such as crystallinity, surface defects and oxidation state to explore the catalytic active sites. Yu *et al.* stated that the amorphous CoSx had transformed into CoOOH after OER, which served as the active species (Fan et al., 2018). In Chen's report, the $FeNi_2S_4$ catalysts had *in situ* reconstructions of FeNi-based hydroxides or oxides (Jiang et al., 2021). Especially, owing to the low intrinsic resistivity, low cost, earth-abundance and high stability, FeS_2 has attracted more attention as a promising catalyst for OER. Although some FeS_2-based catalysts have been reported, the surface structure changing is rarely studied, which is crucial to found the active sites for the FeS_2-based catalysts. Wang *et al.* found that the surface of FeS_2 had self-reconstruction to amorphous/crystalline hybrid FeS_2 after OER (Wang et al., 2021).

Considering the potential practical application, we should make much effort to further improve the catalytic activity and stability of the FeS_2-based catalysts. Among all kinds of constraints, electrical conductivity is one of the most critical factors in electrocatalytic efficiency for improving the activity and stability. Graphene and nano carbons can improve the OER activity and stability of the $FeNi_2S_4$ by integrating with carbon (Jiang et al., 2021). Also, the FeS_2/C nanoparticle has been constructed, and the overpotential at 10 mA cm^{-2} was 240 mV toward OER for the catalyst (Li et al., 2018b). But this report did not concern the surface structure changing after OER. Given the importance of the surface structure, it is necessary to study the surface structure of the FeS_2-C-based catalyst after OER and the synergistic effect of surface structure and introduction of carbon material.

In this paper, serials of FeS_2 and FeS electrocatalysts was prepared by simple two-step method. Meanwhile, a series of FeS_2-450/rGO-x% (x = 5, 10 and 15) catalysts were also prepared using the same method by adding GO in the hydrothermal step. FeS_2-450/rGO-10% showed better catalytic activity and stability than the commercial RuO_2 or FeS_2-450 catalysts. The excellent synergistic effect of surface reconstruction of FeS_2 and the introduction of rGO in FeS_2-450/rGO-10% catalyst were discussed detailed. This will open up new avenues for preparing transition metal disulfide and for their potential practical application.

2. Experimental

2.1. Materials preparation

2.1.1. Preparation of FeS_2 and FeS materials

Typically, 0.6 g Lysine was added to 75 mL $FeCl_3$ solution (0.05 M) and the solution was continuously stirred at 40 °C for 0.5 h. Then, 4 mL $NH_3{\cdot}H_2O$ (32 wt%) was added into the above solution with dropping in 0.5 h. Then, the solution was transferred into a 100 mL Teflon-lined autoclave and heated at 180 °C for 6 h. After cooling to room temperature, the precipitate was filtered, washed and dried at 60 °C for 8 h. After that, the obtained powder and sulfur powder were mixed uniformly with continuous grinding for 0.5 h. Finally, the FeS_2 and FeS samples were obtained by heating the mixed powder to a certain temperature for 4 h in N_2 with a heating rate of 3 °C/min. The samples were marked with FeS_2-400, FeS_2-450, FeS_2-550, FeS-650, and FeS-750, with calcination temperature of 400 °C, 450 °C, 550 °C, 650 °C and 750 °C, respectively.

2.1.2. Preparation of FeS_2-450/rGO-x% (x = 5, 10 and 15) materials

The synthesis procedure of FeS_2-450/rGO-x% (x = 5, 10 and 15) materials is similar to preparing the FeS_2-450 sample, excepting a mount of GO was added into the initial $FeCl_3$ solution. The synthesis process of the FeS_2-450/rGO-x% catalysts has been displayed in Scheme 1 and can be explained according to **Eq. (1) to (3)**. Under the alkaline environment, Fe^{3+} adsorbed on GO converted into Fe_2O_3 during the hydrothermal stage, while the GO was reduced to rGO, forming Fe_2O_3/rGO (**Eqs. (1) and (2)**), as shown in Fig. S1. Under the inert atmosphere of 450 °C, the mixed Fe_2O_3/rGO and S powder transformed into FeS_2-450/rGO and H_2O (**Eq. (3)**). The pieces were marked with FeS_2-450/rGO-5%, FeS_2-450/rGO-10% and FeS_2-450/rGO-15%, with the GO are 0.005, 0.01 and 0.014 g, respectively.

$$NH_3 \cdot H_2O \Longleftrightarrow NH_4^+ + OH^- \quad (1)$$

$$Fe^{3+} + 3OH^- + GO \overset{\text{Hydrothermal}}{\rightarrow} Fe_2O_3/rGO \quad (2)$$

$$Fe_2O_3/rGO + S \overset{\text{inert atmosphere, 450 °C}}{\rightarrow} FeS_2 - 450/rGO + H_2O \quad (3)$$

2.2. Characterizations

The X-ray diffraction patterns(XRD) ranging from 2θ = 20° to 70° were obtained by a powder diffractometer (D8 Advanced, Bruker Co, Germany) with Cu Kα radiation. The surface structure and morphology were characterized by the field emission scanning electron microscope (FESEM, Zeiss Sigma, Japan). The interior structure was obtained by the high-resolution transmission electron microscope (HRTEM, JEOL F200, Japan). The chemical status was acquired by X-ray photoelectron spectroscopy (XPS, ESCALAB 250xi).

2.3. Electrochemical measurements

All the electrochemical measurements were performed using an electrochemical workstation of Gamry with a standard three-electrode system at room temperature. In the three-electrode cell, the Hg/HgO was used as the reference electrode; the graphite rod served as the counter electrode, while the pretreated foam Ni covered with samples was the working electrode. The working electrode was prepared as follows: First, the 10 mg prepared sample was dispersed into a mixture of 1 mL ethanol and 50 μL of Nafion solution (5%, DuPont) with ultrasound for 20 min to get a homogeneous catalyst ink. Second, 100 μL ink was extracted with a micropipette and uniformly dropped onto the pretreated foam Ni (1 × 1 cm^2). Linear sweep voltammetry (LSV) was conducted at a sweep rate of 5 mV s^{-1} by working the voltage range of 0–1 V (*vs* Hg/HgO). All LSV curves were 95% iR-corrected in this paper. The electrochemical double-layer capacitance (C_{dl}) of the samples was calculated by performing the cyclic voltammetry (CV)

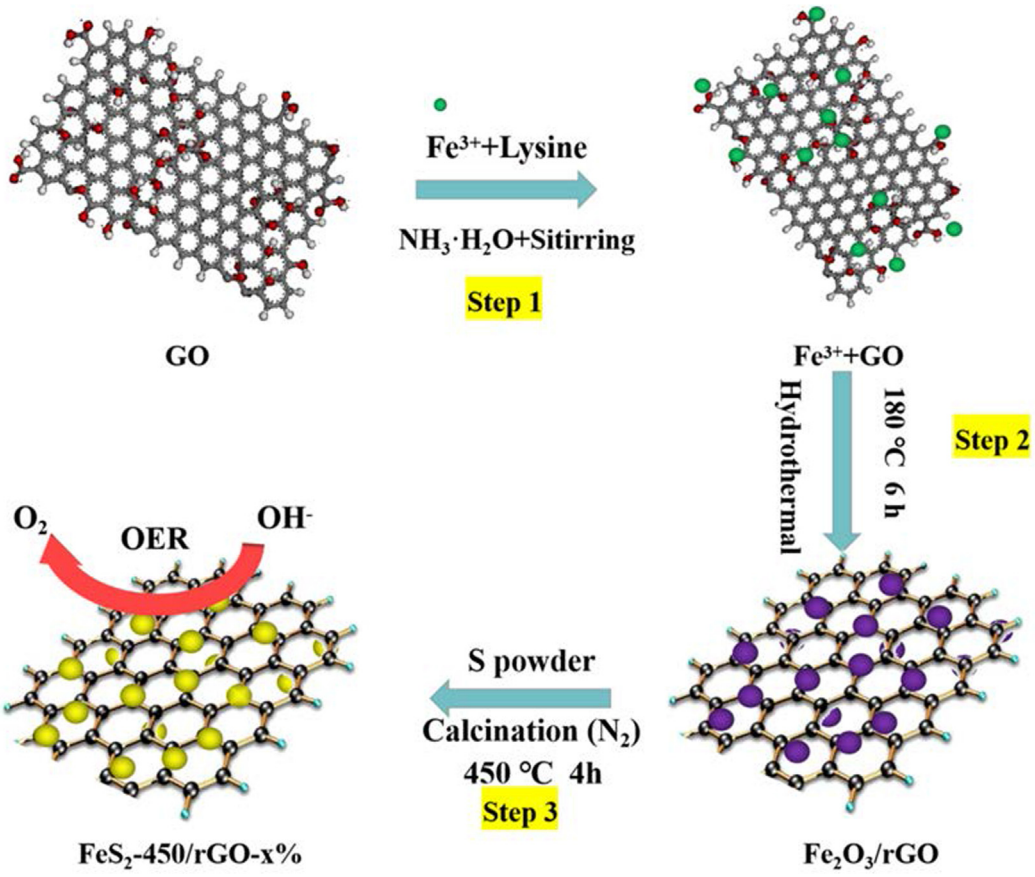

Scheme 1 The synthesis procedure of the FeS_2-450/rGO nanocomposites.

analysis at the scan rates of 20, 40, 60, 80, and 100 mV s^{-1} in 1.0 mol/L (M) KOH. Electrochemical impedance spectroscopy (EIS) was performed in a 0.61 V potentiostatic state with a frequency range of 0.01–100 kHz. The OER stability was carried out using the Chronopotentiometry tests for 18000 s at a potential of 1.527 V *vs* RHE in 1.0 mol/L (M) KOH solution.

All the presented potential in this work was converted to the reversible hydrogen electrode (RHE) potential according to the following two-equation:

$$E(RHE) = \text{potential applied vs. } Hg/HgO + 0.098\,V + 0.0592 \times pH \quad (4)$$

$$\eta = E(RHE) - 1.23\,V \quad (5)$$

Overall water splitting was performed in a two-electrode system, in which FeS_2-450/rGO-10% was the anode electrode while the Pt/C served as the cathode electrode.

3. Results and discussion

3.1. Fabrication and characterization before OER

The phase of FeS_2 and FeS is clearly identified from XRD patterns for the synthesized samples, Fig. 1a. The FeS_2 phase can be observed at 400 °C, 450 °C and 550 °C, where the diffraction lines at 28.52°, 33.05°, 37.08°, 40.77°, 47.43°, 56.28°, 59.01°, 61.69° and 64.29° index to the plans of (111), (200), (210), (211), (220), (311), (222), (023) and (321) of FeS_2 (JCPDS#71–1680), respectively. In contrast, the phases of FeS (JCPDS#89–6926) is found in samples at 650 °C and 750 °C, Fig. 1a.

As reveled by SEM, the FeS_2-400, FeS_2-450 and FeS_2-550 samples are nanospheres with the diameter ranging from 50 to 100 nm, Fig. 2a-d. Among them, the FeS_2-450 exhibits more uniform dispersion and smooth surface, which can facilitate exposure of more active sites to obtain excellent OER performance, Fig. 2b-c. As the temperature increased further, the FeS-650 and FeS-750 samples present irregular micro-scale blocks, which may be caused by aggregation of catalysts, Fig. 2e-f.

3.2. Electrocatalytic performance for OER

The electrocatalytic OER activities of Ni foam, RuO_2, FeS_2-400, FeS_2-450, FeS_2-550, FeS-650 and FeS-750 catalysts were carried out using 1 M KOH as electrolyte (pH = 11.83) at room temperature. The LSV curves show that FeS_2-450 exhibits superior OER performance with smaller potentials and larger current density, indicating the excellent conductivity, as displayed in Fig. 3a. The overpotentials of the Ni foam, RuO_2, FeS_2-400, FeS_2-450, FeS_2-550, FeS-650 and FeS-750 catalysts at 10 mA/cm^2 are 365 mV, 340 mV, 291 mV, 253 mV, 298 mV, 305 mV and 307 mV, respectively, Fig. 3b. Remarkably, the overpotential of FeS_2-450 largely reduced to 253 mV. Further, the overpotentials of the FeS_2-450 at

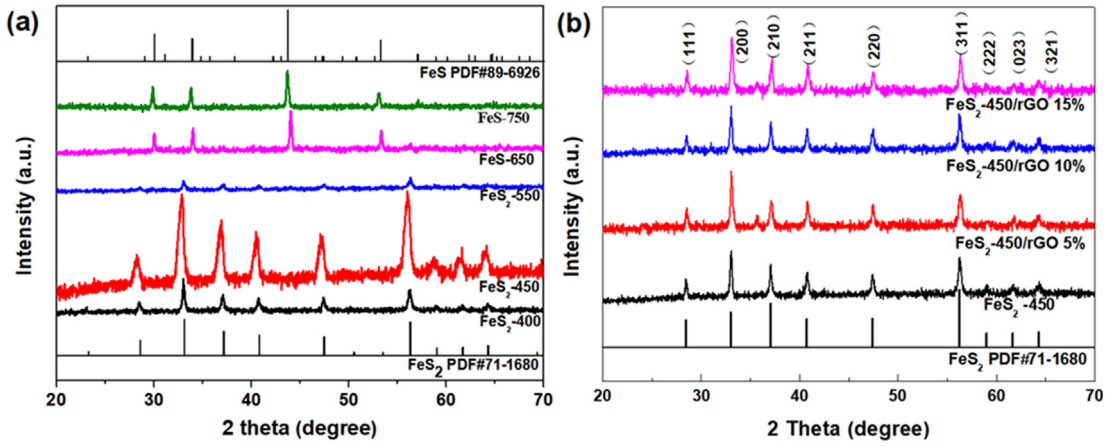

Fig. 1 XRD patterns of prepared samples.

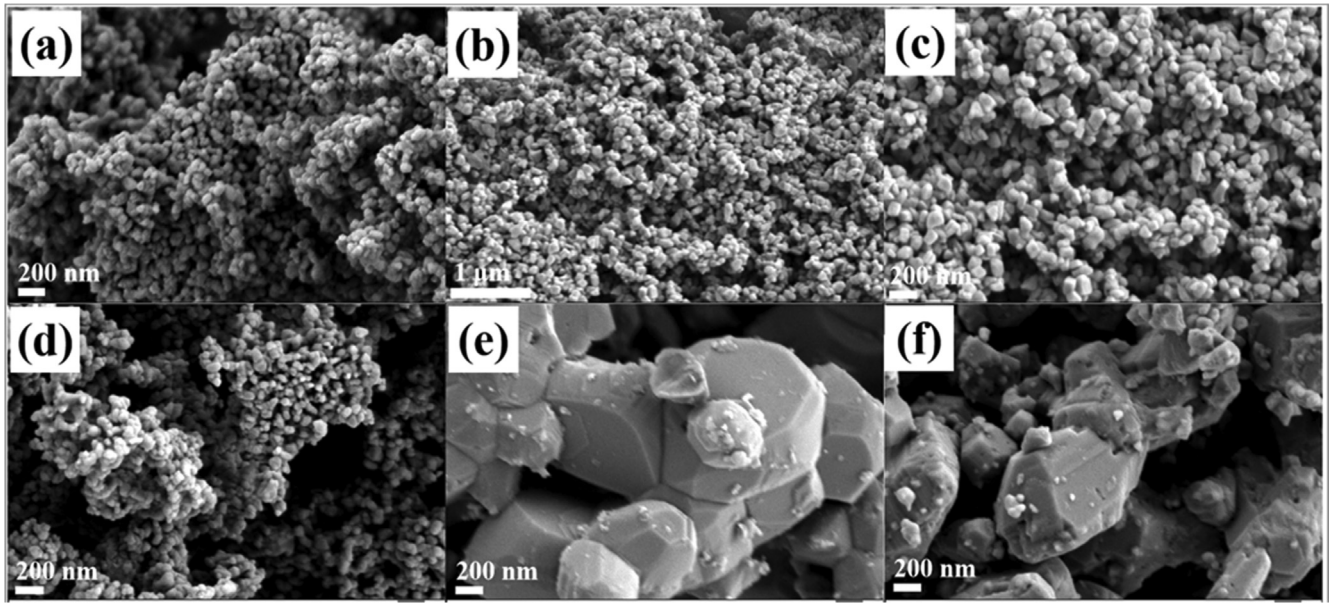

Fig. 2 The SEM images of prepared (a) FeS_2-400 (b,c) FeS_2-450 (d) FeS_2-550 (e) FeS-650 (f) FeS-750.

50 mA/cm^2 and 100 mA/cm^2 are 315 mV and 369 mV, respectively, even superior to commercial precious metal electrocatalyst RuO_2, suggesting the outstanding OER performance. To get insight into understand the intrinsic activity, we calculated the turnover frequency (TOF) of the FeS_2-450, FeS-750 and RuO_2 catalysts at the overpotential of 369 mV and relevant calculation process is provided in the supporting information (Rebekah et al., 2020; Suen et al., 2017). The TOF of the FeS_2-450 reaches 0.311 O_2 per s per site, greater than FeS-750 (0.0114) and RuO_2 (0.0071), demonstrating the highest intrinsic activity in FeS_2-450. All the above results suggest that FeS_2-450 exhibits the best electrocatalytic OER activity in 1 M KOH among these catalysts.

Tafel plots, as a common descriptors to reflect the reaction kinetic of OER, are calculated by the linear formula of $\eta = b \log|j| + a$, Fig. 3c. The Tafel plot of the FeS_2-450 is 72 mV/dec, which is lower than those of Ni foam (243 mV/dec), FeS_2-400 (89.6 mV/dec), FeS_2-550 (74.3 mV/dec), FeS-650 (74.2 mV/dec) and FeS-750 (79.8 mV/dec) catalysts, proving the remarkable OER catalytic kinetics over FeS_2-450. The charge-transfer resistance (R_{ct}) at the catalyst/electrolyte interface are further conducted by the Nyquist plots analysis, Fig. 3d. The decreased order of R_{ct} is FeS_2-450 < FeS_2-400 < FeS_2-550 < FeS-650 < FeS-750, demonstrating accelerated charge-transfer on highly conductive FeS_2-450 (Liu et al., 2019; Li et al., 2021).

The electrochemically active areas (ECSA) are positively correlated to the electric double-layer capacitance (C_{dl}), which can be calculated by the CV curves at different scan rates. The CV curves of Ni-foam, FeS_2-400, FeS_2-450, FeS_2-550, FeS-650 and FeS-750 catalysts were measured in the non-Faraday region at scan rates of 20 mVs^{-1}, 40 mVs^{-1}, 60 mVs^{-1}, 80 mVs^{-1} and 100 mVs^{-1}, Fig. S2. Apparently, the C_{dl} value for FeS_2-450 is 0.45 mFcm^{-2}, significantly larger than that

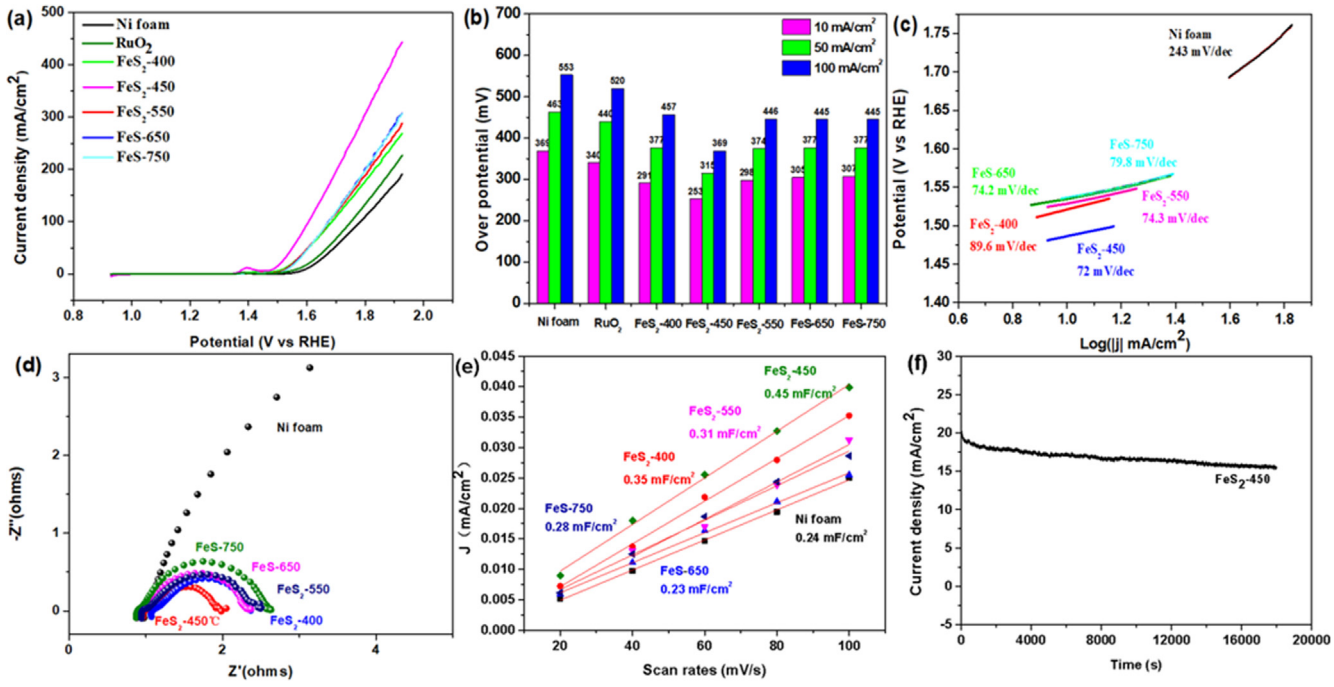

Fig. 3 OER measurement. (a) LSV (b) the overpotentials to achieve current densities of 10, 50, and 100 mA cm^{-2} (c) Tafel plots, (d) Nyquist plots (e) electrochemical double-layer capacitance (C_{dl}) of the prepared Ni foam, FeS_2-400/NF, FeS_2-450/NF, FeS_2-550/NF, FeS-650/NF and FeS-750/NF and (f) i-t cures of FeS_2-450 sample under a constant potential of 1.527 V *vs*. RHE.

of control catalysts, suggesting uniform nanoparticles dispersion of FeS_2-450 offer much more accessible active sites on the surface, Fig. 3e (Shi et al., 2020). The electrochemical OER stability of FeS_2-450 was tested at 1.527 V *vs* RHE in 1 M KOH by chronoamperometry, Fig. 3f. Apparently, FeS_2-450 kept high OER stability within 5 h and without an appreciable current attenuation.

To further enhance the electrocatalytic performance of OER, rGO with high conductivity was introduced to prepared novel FeS_2-450/rGO-x% electrocatalysts. The XRD patterns of FeS_2-450/rGO-x% (x = 5, 10 and 15) samples are displayed in Fig. 1b and corresponding diffraction peaks index to FeS_2, consistent with fabricated FeS_2 at the same calcination temperature. The morphology and microstructure of the FeS_2-450/rGO-10% catalyst was characterized by the SEM, TEM and HRTEM. The SEM indicates that the FeS_2-450/rGO-10% is composed of FeS_2-450 nanoparticles and rGO nanosheets and FeS_2-450 nanoparticles are relatively uniformly dispersed on the surface of rGO nanosheets by zoom-in SEM image, Fig. 4a-c. The elemental mapping images reveals Fe and S ele-

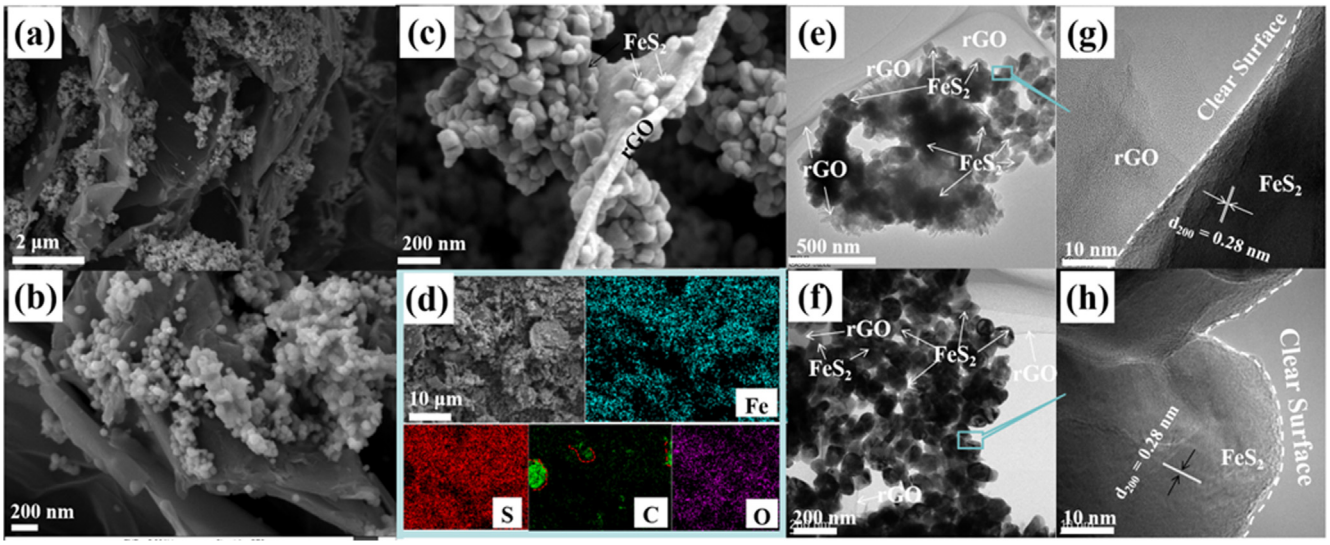

Fig. 4 (a-c) SEM images, (d) EDX surface mapping scans, (e, f) TEM and (g, h) HRTEM images of the prepared FeS_2-450/rGO-10% sample.

ments are homogeneously distributed, while the elemental mapping image of exposed trace C further confirms that rGO has been surrounded by the FeS_2, which is conducive to accelerate electron transfer and improve catalytic activity, Fig. 4d. TEM images of FeS_2-450/rGO-10% verified that the catalyst is composed of nanoparticle and nanosheets, Fig. 4e-f. Moreover, the FeS_2-450 in FeS_2-450/rGO-10% has a clear surface and the lattice fringes with plane distances of 0.280 nm are assigned to (200) interplanar spacing of FeS_2, Fig. 4g-h.

The OER activity of the FeS_2-450/rGO-5%, FeS_2-450/rGO-10% and FeS_2-450/rGO-15% catalysts were also evaluated by LSV using 1.0 M KOH electrolyte and the corresponding overpotentials were displayed in Fig. 5a, b, with Ni foam, RuO_2 and FeS_2-450 as the contrast. Remarkably, the overpotentials of FeS_2-450/rGO-10% at current density of 10 mA/cm^2, 50 mA/cm^2, and 100 mA/cm^2 are 140 mV, 310 mV and 370 mV, respectively, significantly lower than the commercial RuO_2, FeS_2-450 and previous Fe/S-based catalysts toward OER in Table 1, indicating the outstanding OER performance after introducing highly conductive rGO. Compared with FeS_2-450 (73 mV/dec), FeS_2-450/rGO-10% showed a lower Tafel slope (71 mV/dec), demonstrating that the rGO accelerate the reaction kinetics, Fig. 5c. The The order of R_{ct} values is FeS_2-450/rGO-10% < FeS_2-450/rGO-15% < FeS_2-450 < FeS_2-450/rGO-5% < RuO_2 < Ni foam, indicating that FeS_2-450/rGO-10% has the minimum charge transfer resistance for OER, Fig. 5d. Moreover, the CV curves of Ni-foam, FeS_2-450, FeS_2-450/rGO-5%, FeS_2-450/rGO-10% and FeS_2-450/rGO-15% catalysts in the non-Faraday region at different scan rates (20 mVs^{-1}, 40 mVs^{-1}, 60 mVs^{-1}, 80 mVs^{-1} and 100 mVs^{-1}) were presented in Fig. S3. FeS_2-450/rGO-10% achieved the maximum C_{dl} value of 1.71 mF cm^{-2}, which could be assigned to enhanced electron transport between the active sites and the electrolyte owing to the importing of rGO, Fig. 5e. The i-t curve in Fig. 5f shows that FeS_2-450/rGO-10% catalyst kept OER stability within 5 h without an appreciable current attenuation and the current density is higher than that of FeS_2-450 in Fig. 3f.

As discussed above, the FeS_2-450/rGO-10% presents superior electrocatalytic performance toward OER. Meanwhile, an electrolyzer in a two-electrode FeS_2-450/rGO-10%/NF//Pt/C/NF was assembled in 1 M KOH for the overall water splitting, while the RuO_2/NF//Pt/C/NF and Ni foam//Ni foam system as the comparison. As expected in Fig. 6a and b, the voltage at 10 mA cm^{-2} for the FeS_2-450/rGO-10%/NF//Pt/C/NF system is 1.52 V, significantly better than those of RuO_2/NF//Pt/C/NF (1.55 V) and Ni foam//Ni foam (1.86 V) systems, indicating that the FeS_2-450/rGO-10%/NF//Pt/C/NF system possess higher electrocatalytic activity toward overall water splitting.

3.3. Characterization after OER

To get insight to understand the OER catalytic activity and stability, a systematic investigation of the catalyst after OER was conducted. The FeS_2-450/rGO-10% catalyst after stability test maintain nanoparticles and nanosheets morphology, Fig. 7a-e, demonstrating its high stability. Moreover, the elemental mapping of catalysts after OER in Fig. 7c indicates the uniform distribution of Fe, S, C, and O elements. It is worth noting that the clear surface of catalyst disappeared con-

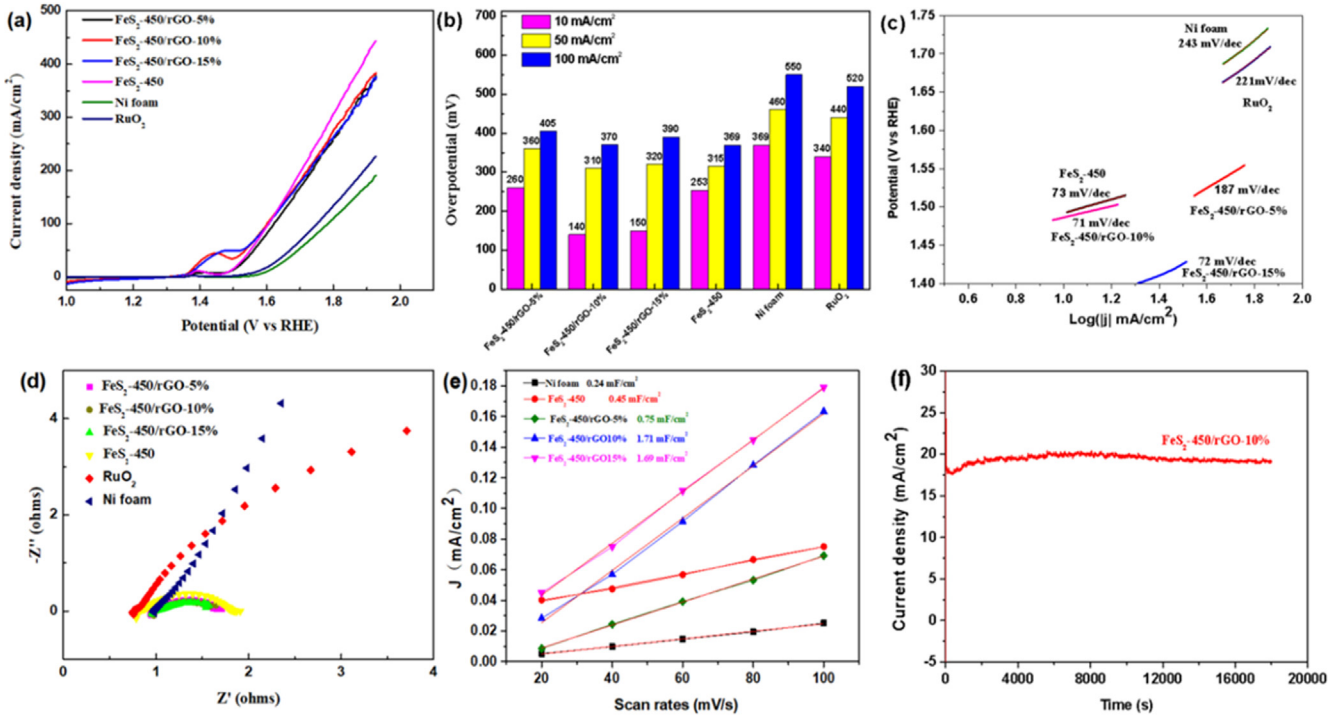

Fig. 5 OER measurement. (a) LSV, (b) the overpotentials to achieve current densities of 10, 50, and 100 mA cm^{-2}, (c) Tafel plots, (d) Nyquist plots (e) electrochemical double-layer capacitance (C_{dl}) of the prepared Ni foam, FeS_2-450/NF, FeS_2-450/rGO-5%/NF, FeS_2-450/rGO-10%/NF and FeS_2-450/rGO-15%/NF and (f) I-t curve of FeS_2-450/rGO-10% under a constant potential of 1.527 V *vs.* RHE.

Table 1 The OER activity of the FeS_2-450/rGO-10% in this work, compared with some state-of-the-art Fe/S-based OER electrodes in alkaline media reported in previous references.

Catalysts	Electrolyte	η/mV10 mA cm^{-2}	Tafel slope/mV dec^{-1}	References
FeS_2/C	1 M KOH	291	65.6	Pan et al., 2019
Fe_7S_8	1 M KOH	270	43	Chen et al., 2017
Fe_7S_8/FeS_2/C-20	1 M KOH	262	48	Li et al., 2018a
$FeNi_2S_4$	1 M KOH	405	126	Jiang et al., 2021
Pyrite FeS_2/C	1 M KOH	240	92	Li et al., 2018b
FeS_2	1 M KOH	189.5	71	Wang et al., 2021
$Fe_{0.8}Ni_{0.15}S_{1.05}$	1 M KOH	228	53	Jing et al., 2020
$Ni_{0.7}Fe_{0.3}S_2$	1 M KOH	198	109	Yu et al., 2017
FeS_2/$CoNiSe_2$	1 M KOH	230	54	Yang et al., 2022
FeS_2-450/rGO-10%	1 M KOH	140	71	This work

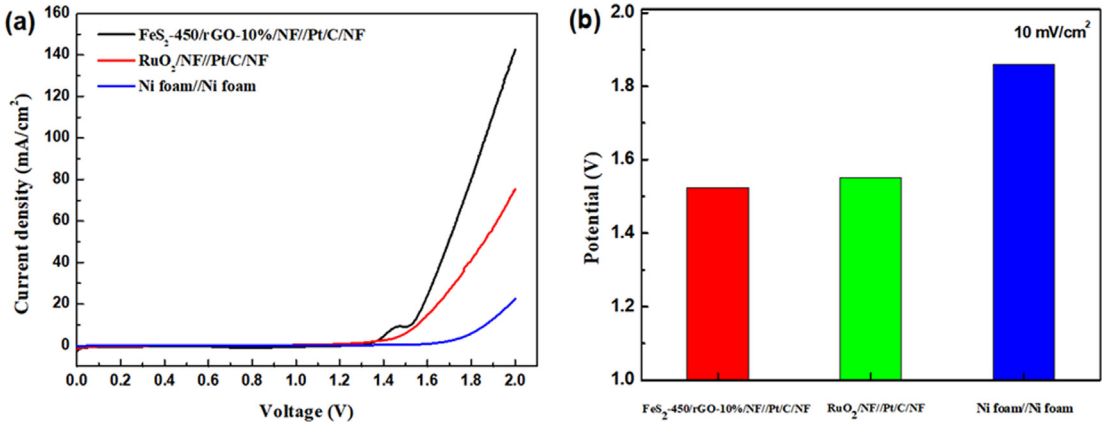

Fig. 6 (a) LSV curves of FeS_2-450/rGO-10%/NF//Pt/C/NF, RuO_2/NF//Pt/C/NF and Ni foam//Ni foam and (b) the corresponding potential at current densities of 10 mA cm^{-2} under a constant potential of 1.6 V.

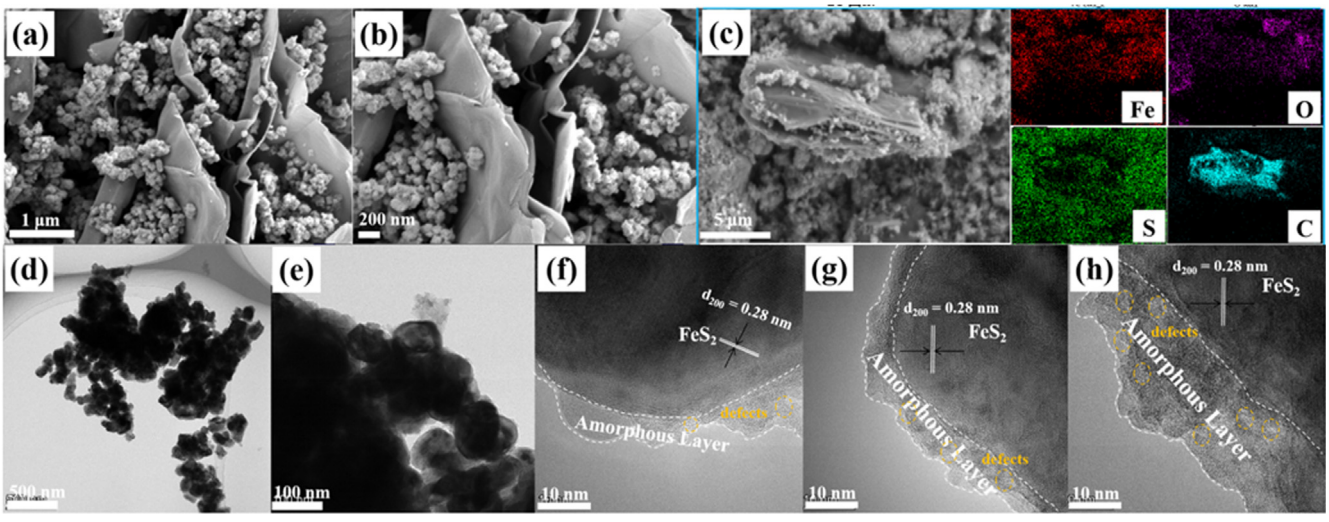

Fig. 7 (a, b) SEM images, (c) EDX surface mapping scans, (d, e) TEM and (f-h) HRTEM images of the prepared FeS_2-450/rGO-10% after OER.

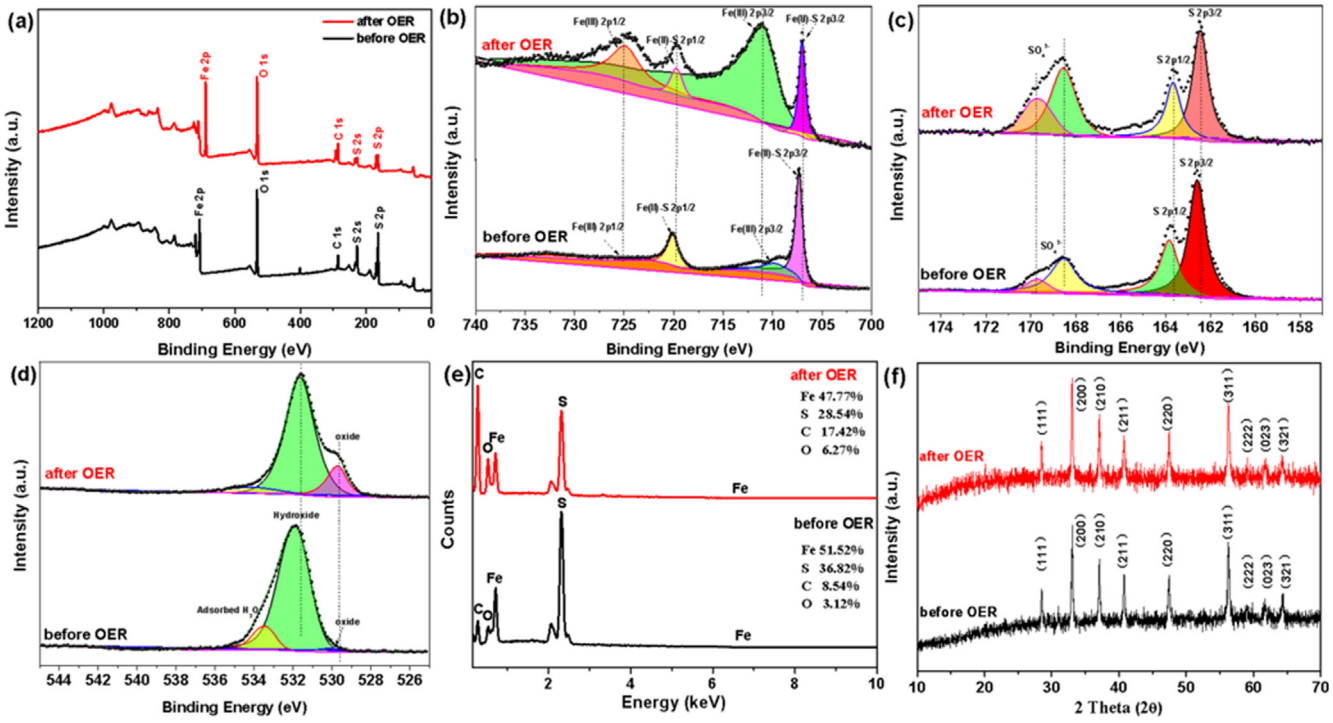

Fig. 8 XPS spectra of (a) survey (b) Fe 2p (c) S 2p (d) O 2p (e) the percentages of Fe, S, C and O with the prepared FeS_2-450/rGO-10% before and after OER and (f) XRD with the prepared FeS_2-450/rGO-10% before and after OER.

siderably, although lattice fringes with plane distances of 0.280 nm is also assigned to (200) interplanar spacing of FeS_2. At the same time, an amorphous layer with some defects appeared, which may be associated with Fe oxo/hydroxide species or S defects, implying the surface reconstruction of the catalyst.

To figure out the structure and electronic structure of the catalyst before and after stability test, we have performed a series of studies, Fig. 8. First, the chemical state of the catalyst before and after the reaction was investigated through XPS. The full spectrum in Fig. 8a suggests the coexistence of Fe 2p, S 2p, O 1s and C 1s elements. The binding energies at 707.5 eV and 720.3 eV assigned to the $Fe_{(II)}$-S 2p3/2 and Fe $_{(II)}$-S 2p1/2 while the other two peaks at 712.3 eV and 725.9 eV belong to the Fe^{3+}(Chen et al., 2022), and the latter could be assigned to Fe-OOH bonds, Fig. 8b. The peaks intensity and area of Fe^{3+} after OER is dramatically stronger and larger compared to catalyst before the reaction, indicating the formation of Fe-oxo/hydroxide species during the catalytic process (Yu et al., 2017), Fig. 8b. The binding energies at 163.0 eV and 164. eV can ascribe to S $2p_{3/2}$ and S $2p_{1/2}$ in metal sulfide, while the two peaks at 168.4 eV and 169.7 eV belong to sulfate (Wang et al., 2017), resulting from particle oxidation of FeS_2, Fig. 8c. The peak at 529.8 eV belonging to O^{2-} (lattice O) after OER became more vigorous, which is consistent with the increased peak of Fe-OOH bonds, further confirming the existence of Fe-oxo/hydroxide species and surface reconstruction of the catalyst, Fig. 8d.

On the other hand, the comparison of EDX elemental analysis before and after the reaction clearly shows that the S relative content sharply reduced, in Fig. 8e. In contrast, the O content increased after OER, further verifying the surface reconstruction of catalysts, which is consistent with the above discussion in XPS. In addition, XRD was used to characterize the phase composites of the catalysts before and after OER. No significant difference was found in FeS_2-450/rGO-10% after OER compared with that of before OER, suggesting that the FeS_2 in FeS_2-450/rGO-10% catalyst kept its phase and the reconstruction of the catalyst only occurred on the surface, Fig. 8f.

4. Conclusion

Thanks to the integration of FeS_2 and highly conductive rGO, the FeS_2-450/rGO-10% exhibited the best catalytic activity toward OER with an ultra-low overpotential of 140 mV and a smaller Tafel slope of 71 mV/dec and better stability than FeS_2-450 and commercial RuO_2. As discussed above, the enhanced catalytic activity originated from the synergistic effect of surface reconstruction of FeS_2 and rGO, in which the surface of FeS_2 functions as catalytic active sites because of the reconstruction of the structure and chemical state and rGO serves as effective electron transfer channel at the catalyst/electrolyte interface. This facile synthetic strategy of excellent electrocatalytic performance for OER toward overall water splitting opens new avenues for potential practical application.

CRediT authorship contribution statement

Xiaozhen Ren: Conceptualization, Methodology, Writing - original draft, Writing - review & editing, Supervision. **Hua Yang:** Conceptualization, Methodology, Writing - review & editing, Supervision.

Declaration of Competing Interest

The authors declare that they have no known competing financial interests or personal relationships that could have appeared to influence the work reported in this paper.

Acknowledgements

This work was supported by the Natural Science Foundation of Shandong Province (ZR2021QE086) and the Undergraduate Innovation Training Program Fund of Liaocheng University (Grant No. cxcy2022247).

Appendix A. Supplementary material

Supplementary data to this article can be found online at https://doi.org/10.1016/j.arabjc.2023.105069.

References

Audichon, T., Napporn, T.W., Canaff, C., Morais, C., Comminges, C., Kokoh, K.B., 2016. IrO_2 coated on RuO_2 as efficient and stable electroactive nanocatalysts for electrochemical water splitting. J. Phys. Chem. C. 120 (5), 2562–2573. https://doi.org/10.1021/acs.jpcc.5b11868.

Chen, S.C., Kang, Z.X., Zhang, X.D., Xie, J.F., Wang, H., Shao, W., et al, 2017. Highly active Fe sites in ultrathin pyrrhotite Fe_7S_8 nanosheets realizing efficient electrocatalytic oxygen evolution. ACS Cent. Sci. 3 (11), 1221–1227. https://doi.org/10.1021/acscentsci.7b00424.

Chen, L., Wang, Y.P., Zhao, X., Wang, Y., Li, Q., Wang, Q., et al, 2022. Trimetallic oxyhydroxides as active sites for large-current-density alkaline oxygen evolution and overall water splitting. J. Mater. Sci. Technol. 110, 128. https://doi.org/10.1016/j.jmst.2021.08.083.

Fan, K., Zou, H.Y., Lu, Y., Chen, H., Li, F.S., Liu, J.X., et al, 2018. Direct observation of structural evolution of metal chalcogenide in electrocatalytic water oxidation. ACS Nano 12 (12), 12369. https://doi.org/10.1021/acsnano.8b06312.

Gao, M., Sheng, W., Zhuang, Z., Fang, Q., Gu, S., Jiang, J., et al, 2014. Efficient water oxidation using nanostructured α-Nickel-hydrixide as an electrocatalyst. J. Am. Chem. Soc. 136 (19), 7077–7084. https://doi.org/10.1021/ja502128j.

Jiang, J., Zhang, Y.J., Zhu, X.J., Lu, S., Long, L.L., Chen, J.J., 2021. Nanostructured metallic $FeNi_2S_4$ with reconstruction to generate FeNi-based oxide as a highly-efficient oxygen evolution electrocatalyst. Nano Energy 81,. https://doi.org/10.1016/j.nanoen.2020.105619 105619.

Jin, K., Park, J., Lee, J., Yang, K.D., Pradhan, G.K., Sim, U., et al, 2014. Hydrated Manganese(II) Phosphate $(Mn_3(PO_4)_2{\cdot}3(H_2O)$ as a water oxidation catalyst. J. Am. Chem. Soc. 136, 7435–7443. https://doi.org/10.1021/ja5026529.

Jing, Z.X., Zhao, Q.Y., Zheng, D.H., Sun, L., Geng, J.H., Zhou, Q.N., et al, 2020. Nickel-doped pyrrhotite iron sulfide nanosheets as a highly efficient electrocatalyst for water splitting. J. Mater. Chem. A. 8, 20323–20330. https://doi.org/10.1039/D0TA07624D.

Li, R., Li, Y., Yang, P., Ren, P., Wang, D., Lu, X., et al, 2022. Synergistic interface engineering and structural optimization of non-noble metal telluride-nitride electrocatalysts for sustainably overall seawater electrolysis. Appl. Catal. B: Environ. 318,. https://doi.org/10.1016/j.apcatb.2022.121834 121834.

Li, Z.C., Xiao, M.M., Zhou, Y., Zhang, D.L., Wang, H.Z., Liu, X., et al, 2018b. Pyrite FeS_2/C nanoparticles as an efficient bifunctional catalyst for overall water splitting. Dalton Trans. 47, 14917–14923. https://doi.org/10.1039/c8dt02927j.

Li, Y., Yin, J., An, L., Lu, M., Sun, K., Zhao, Y., et al, 2018a. FeS_2/CoS_2 interface nanosheets as efficient bifunctional electrocatalyst for overall water splitting. Small 14, 1801070. https://doi.org/10.1002/smll.201801070.

Li, Y., Yin, Z., Cui, M., Liu, X., Xiong, J., Chen, S., et al, 2021. Interface engineering of transitional metal sulfide–MoS_2 heterostructure composites as effective electrocatalysts for water-splitting. J. Mater. Chem. A 9, 2070–2092. https://doi.org/10.1039/D0TA10815D.

Liu, Y., Jiang, S., Li, S., Zhou, L., Li, Z., Li, J., et al, 2019. Interface engineering of (Ni, Fe)$_S$2@Mo$_S$2 heterostructures for synergetic electrochemical water splitting. Appl. Catal. B: Environ. 247, 107–114. https://doi.org/10.1016/j.apcatb.2019.01.094.

Pan, K., Zhai, Y., Zhang, J., Yu, K., 2019. FeS_2/C nanowires as an effective catalyst for oxygen evolution reaction by electrolytic water splitting. Materials 12 (20), 3364. https://doi.org/10.3390/ma12203364.

Rebekah, A., Anantharaj, S., Viswanthan, C., Ponpandian, N., 2020. Zn-substituted $MnCo_2O_4$ nanostructure anchored over rGO for boosting the electrocatalytic performance towards methanol oxidation and oxygen evolution reaction (OER). Int. J. Hydrogen Energy. 45 (29), 14713–14727. https://doi.org/10.1016/j.ijhydene.2020.03.231.

Ren, X., Li, X., Peng, Y., Wang, G., Yin, J., Zhao, X., et al, 2022. $FeNiS_2$/reduced graphene oxide electrocatalysis with reconstruction to generate FeNi oxo/hydroxide as a highly-efficient water oxidation electrocatalyst. Rare Metals 41 (12), 4127–4137. https://doi.org/10.1007/s12598-022-02104-z.

Roy, S., Bagchi, D., Dheer, L., Sarma, S.C., Peter, S.C., 2021. Mechanistic insights into the promotional effect of Ni substitution in non-noble metal carbides for highly enhanced water splitting. Appl. Catal. B: Environ. 298,. https://doi.org/10.1016/j.apcatb.2021.120560 120560.

Shi, M., Zhang, Y., Zhu, Y., Wang, W., Wang, C., Yu, A., et al, 2020. A flower-like CoS_2/MoS_2 heteronanosheet array as an active and stable electrocatalyst toward the hydrogen evolution reaction in alkaline media. RSC Adv. 10, 8973–8981. https://doi.org/10.1039/C9RA10963C.

Suen, N.T., Hung, S.F., Quan, Q., Zhang, N., Xu, Y., Chen, H., 2017. Electrocatalysis for the oxygen evolution reaction: recent development and future perspectives. Chem. Soc. Rev. 46, 337–365. https://doi.org/10.1039/C6CS00328A.

Wang, J., Bai, F., Chen, X., Lu, Y., Yang, W., 2017. Intercalated Co$(OH)_2$-derived flower-like hybrids composed of cobalt sulfifide nanoparticles partially embedded in nitrogendoped carbon nanosheets with superior lithium storage. J. Mater. Chem. 5, 3628–3637. https://doi.org/10.1039/C6TA10151H.

Wang, X., Huang, H., Qian, J., Li, Y., Shen, K., 2023. Intensified Kirkendall effect assisted construction of double-shell hollow Cu-doped CoP nanoparticles anchored by carbon arrays for water splitting. Appl. Catal. B: Environ. 325,. https://doi.org/10.1016/j.apcatb.2022.122295 122295.

Wang, G., Jin, C., Zhang, G., Qian, L., Chen, X., Tan, J., et al, 2021. Surface self-reconstructed amorphous/crystalline hybrid iron disulfifide for high-effififficiency water oxidation electrocatalysis. Dalton Trans. 50, 6333–6342. https://doi.org/10.1039/D1DT00730K.

Wu, H.H., Wang, J., Wang, G.X., Cai, F., Ye, Y., Jiang, Q., et al, 2016. High-performance bifunctional oxygen electrocatalyst derived from iron and nickel substituted perfluorosulfonic acid/polytetrafluoroethylene copolymer. Nano Energy 30, 801–809. https://doi.org/10.1016/j.nanoen.2016.09.016.

Wu, J., Zhang, Q., Shen, K., Zhao, R., Zhong, W., Yang, C., et al, 2022. Modulating interband energy separation of boron-doped Fe_7S_8/FeS_2 electrocatalysts to boost alkaline hydrogen evolution reaction. Adv. Funct. Mater. 32, 2107802. https://doi.org/10.1002/adfm.202107802.

Xu, Y., Feng, T., Cui, Z., Guo, P., Wang, W., Li, Z., 2021. Fe_7S_8/FeS_2/C as an efficient catalyst for electrocatalytic water splitting. Int. J. Hydrogen Energy. 46, 39216–39225. https://doi.org/10.1016/j.ijhydene.2021.09.159.

Yang, J., Xuan, H., Yang, J., Meng, L., Wang, J., Liang, X., et al, 2022. Metal-organic framework-derived FeS_2/$CoNiSe_2$ heterostructure nanosheets for highly-efficient oxygen evolution reaction. Appl. Surf. Sci. 578,. https://doi.org/10.1016/j.apsusc.2021.152016 152016.

Yu, J., Cheng, G., Luo, W., 2017. Ternary nickel-iron sulfide microflowers as a robust electrocatalyst for bifunctional water splitting. J. Mater. Chem. A 5, 15838–15844. https://doi.org/10.1039/C7TA04438K.